Photoacoustics 40 (2024) 100657

Contents lists available at ScienceDirect

Photoacoustics

journal homepage: www.elsevier.com/locate/pacs

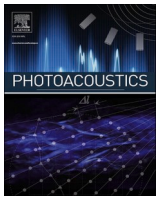

Miniature optical fiber photoacoustic spectroscopy gas sensor based on a 3D micro-printed planar-spiral spring optomechanical resonator

Taige Li [a,1], Pengcheng Zhao [a,1], Peng Wang [a], Kummara Venkata Krishnaiah [a], Wei Jin [a,*], A. Ping Zhang [a,b,**]

[a] Photonics Research Institute, Department of Electrical and Electronic Engineering, The Hong Kong Polytechnic University, Kowloon, Hong Kong SAR
[b] State Key Laboratory of Ultraprecision Machining Technology, The Hong Kong Polytechnic University, Kowloon, Hong Kong SAR

ARTICLE INFO

Keywords:
Optical fiber sensor
Photoacoustic gas sensor
Optomechanical microresonator
Fabry-Pérot cavity
3D micro-printing

ABSTRACT

Photoacoustic spectroscopy (PAS) gas sensors based on optomechanical resonators (OMRs) have garnered significant attention for ultrasensitive trace-gas detection. However, a major challenge lies in balancing small size with high performance when developing ultrasensitive miniaturized optomechanical resonant PAS (OMR-PAS) gas sensors for space-constrained applications. Here, we present a miniature optical fiber PAS gas sensor based on a planar-spiral spring OMR (PSS-OMR) that is *in situ* 3D micro-printed on the end-face of a fiber-optic ferrule. Experimental results demonstrate that mechanical vibrational resonance can enhance the sensor's acoustic sensitivity by over two orders of magnitude. Together with a 1.4 μL non-resonant photoacoustic cell, it can detect C_2H_2 gas concentration at the 45-ppb level, and its response is very fast approximating 0.2 seconds. This optical fiber OMR-PAS gas sensor holds great promise for the detection or monitoring of rapidly varying trace gas in many applications ranging from production process control to industrial environmental surveillance.

1. Introduction

Gas sensors capable of detecting the concentration of gaseous species play crucial roles in a wide range of applications, such as industrial safety, agricultural production control, and environmental monitoring [1–3]. Optical gas sensors based on laser absorption spectroscopy (LAS) have become an indispensable trace-gas monitoring technology because of their advantages of fast response, high sensitivity, and high selectivity [4–6]. One of the most sensitive and robust LAS gas sensing technologies is photoacoustic spectroscopy (PAS), in which a modulated laser beam whose wavelength matching with an absorption line of a target gas species can generate a weak acoustic wave and then the quantitative sensing of the gas's concentration can be accomplished via the detection of the generated acoustic signals [7–10]. Different to many other optical sensors, PAS gas sensors do not need expensive optical spectrum analysing instruments, but acoustic sensors such as microphones. Therefore, PAS has gradually become one of most competitive gas sensor technologies because of its relatively concise structure and the wide availability of acoustic sensors [11–16].

The performance of a PAS gas sensor is primarily determined by the capability of its acoustic sensor in the detection of weak photoacoustic (PA) signals. To achieve high signal-to-noise ratio (SNR) and high sensitivity, resonant acoustic sensors have been widely employed in PAS gas sensors in which very weak PA signals can be detected via a resonance amplification mechanism. For instance, quartz-enhanced photoacoustic spectroscopy (QEPAS) uses a quartz tuning fork as a resonant acoustic sensor that can accumulate acoustic energy to detect very weak PAS signals [17,18]. Because of many remarkable advantages such as fast response and high SNR, many variants of QEPAS sensors have been developed for on-line monitoring of a variety of gases [19–21]. However, conventional QEPAS sensors usually utilize piezoelectric effect for signal readout, which may limit their wide use especially for remote sensing in harsh environments. Recently, optical fiber has been used to create a Fabry-Pérot (FP) micro-interferometer with a quartz tuning fork to enable fiber-optic interferometric readout with remote sensing ability [22]. However, the size of such quartz tuning fork-based sensor heads is

* Corresponding author.
** Corresponding author at: Photonics Research Institute, Department of Electrical and Electronic Engineering, The Hong Kong Polytechnic University, Kowloon, Hong Kong SAR.
E-mail addresses: eewjin@polyu.edu.hk (W. Jin), azhang@polyu.edu.hk (A.P. Zhang).
[1] These authors contributed equally to this work.

https://doi.org/10.1016/j.pacs.2024.100657
Received 3 October 2024; Received in revised form 23 October 2024; Accepted 23 October 2024
Available online 24 October 2024

typically at the centimeter scale, which restricts their applications in space-restricted circumstances.

These obstacles can be overcome by using optical fiber-based PAS sensor technologies, in which optical fiber is used to deliver the excitation laser beam and a small acoustic transduction element, such as diaphragm [23–25] or cantilever [26–28], is utilized to detect PAS signals. Diaphragm is the most typical element used to form a FP interferometric cavity at the output end of an optical fiber for acoustic sensing, and therefore it is also widely used for optical fiber PAS sensors. For example, Tan et al. demonstrated an optical fiber acoustic sensor using a graphene diagram-based nano-mechanical resonator for PAS gas sensing [23]. Enhanced by the resonance of diagram, the optical fiber PAS sensor can detect C_2H_2 gas at the level of 119.8 parts-per-billion (ppb). However, the diaphragm-based acoustic sensors have relatively less flexibility in tailoring mechanical resonances. In a similar graphite diaphragm-based optical fiber PAS sensor developed by Fan et al. [25], no resonant signal amplification was observed in the range of operation, though a highly-reflective Au film-based multi-pass cell enabled the sensor to detect C_2H_2 gas at the level of ~50 ppb.

Recently, cantilever-based PAS technology, typically called as cantilever-enhanced photoacoustic spectroscopy (CEPAS), has attracted remarkable attention because of its more flexibility in tailoring mechanical resonances for PAS signal enhancement. For instance, Zhou et al. proposed a fiber-optic CEPAS sensor based on a borosilicate glass micromirror that is freely hanged by an over 2-mm long cantilever beam [26]. Operating at resonant frequency, the optical fiber CEPAS sensor achieved a noise-equivalent concentration of 15 ppb in the detection of C_2H_2 gas. However, as the sensor was assembled with three stages, its size is relatively bulky and at the centimeter scale. Guo et al. demonstrated another CEPAS sensor using a silicon cantilever-based fiber-optic FP interferometric acoustic sensor [28]. Enhanced by the resonance of the silicon cantilever and a non-resonant photoacoustic cell (PAC), the sensor achieved remarkably high sensitivity and can detect C_2H_2 gas at a level as low as 199.8 parts per trillion (ppt). However, as the sensitivity of a CEPAS sensor depends on very much the length of cantilever and the sensor head was mechanically assembled, its size is also at the centimeter scale, i.e., with a length of 2 cm and a diameter of 1 cm, which poses limitations for space-constrained applications.

The abovementioned obstacle can be potentially overcome by using our recently proposed spirally-suspended optomechanical microresonator (OMR) [29]. It was demonstrated that a spiral design of cantilever can tackle the trade-off between small size and high sensitivity to develop ultrasmall optical fiber-tip acoustic sensors. In this work, we extend the design to develop a ferrule-top planar-spiral spring OMR (PSS-OMR) for highly sensitive PAS gas sensing, as shown in Fig. 1.

Compared to the optical fiber end-face, the fiber-optic ferrule end-face is also an inherently light-coupled platform but offers a larger area that allows for the fabrication of a larger suspended disk bearing acoustic waves and longer spring arms to enhance sensitivity. Experimental results revealed that different ferrule-top PSS-OMRs with customizable size and tunable resonant frequency can be directly printed by using an in-house optical 3D micro-printing technology. Together with a non-resonant photoacoustic cell, the fabricated optical fiber optomechanical resonant PAS (OMR-PAS) sensor can detect the concentration of C_2H_2 gas at the 45-ppb level at the frequency of ~15 kHz and its response time is as short as 0.2 seconds.

2. Materials and methods

2.1. Materials

EPON SU-8 resin purchased from HEXION Ltd. was used for the 3D micro-printing of PSS-OMR sensors. The solid epoxy was dissolved in cyclopentanone purchased from Aladdin Scientific Corp. at the weight ratios of 15 % and 25 % for the bottom and upper layers, respectively. 4-Octyloxydiphenyliodonium hexafluoroantimonate (OPPI) purchased from Arctom Scientific company and tributylamine (TBA) purchased from Meryer Chemical Technology Co., Ltd were used as a photoinitiator and an inhibitor at a weight percentage of 4 % and 0.5 %, respectively, with respect to SU-8 resin. 2-(2H-Benzotriazol-2-yl)-4,6-bis(1-methyl-1-phenylethyl)phenol purchased from J&K Scientific, also known as Tinuvin 234, was added into the photoresist as a UV absorption agent, at a weight percentage of 0.4 % with respect to SU-8 resin in the fabrication of the upper layer of PSS-OMRs.

2.2. 3D micro-printing of optical fiber ferrule-top PSS-OMRs

The optical 3D micro-printing processes are shown in Fig. 2, which include two rounds of repeated processes for the bottom and upper layers, respectively. Firstly, a dip coating was applied to deposit SU-8 photoresist on the end face of a fiber-optic ferrule. The sample was then soft-baked in an oven at 65 °C for 5 minutes and followed by 95°C for 15 minutes to evaporate solvent. After soft-baking, a machine vision-assisted maskless UV exposure process was applied to pattern SU-8 photoresist. Image data was sliced from a 3D model of the designed structure and then loaded to DMD board to dynamically generate UV patterns for a dynamic exposure process. After exposure, the sample was post-baked by using a blast drying oven at 65 °C for 40 minutes. Finally, the sample was developed by propylene glycol monomethyl ether acetate (PGMEA) and then cleaned by using a low surface tension solvent

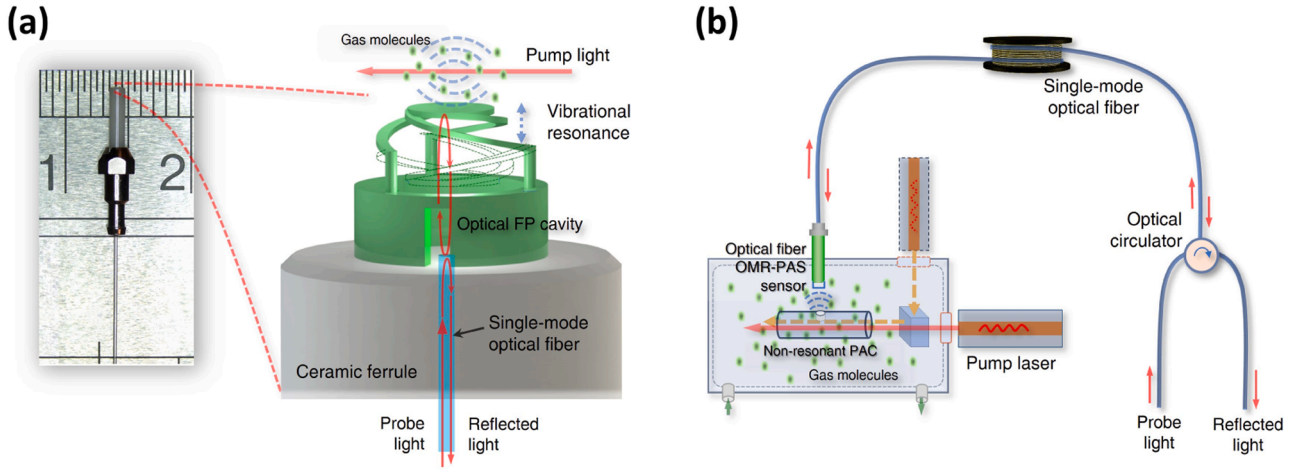

Fig. 1. Schematics of an optical fiber OMR-PAS gas sensor and its application in a PAS trace-gas detection microsystem. **(a)** Schematic design of an optical fiber OMR-PAS gas sensor based on a ferrule-top PSS-OMR. **(b)** Schematic of a non-resonant PAC enhanced optical fiber PAS trace-gas detection microsystem.

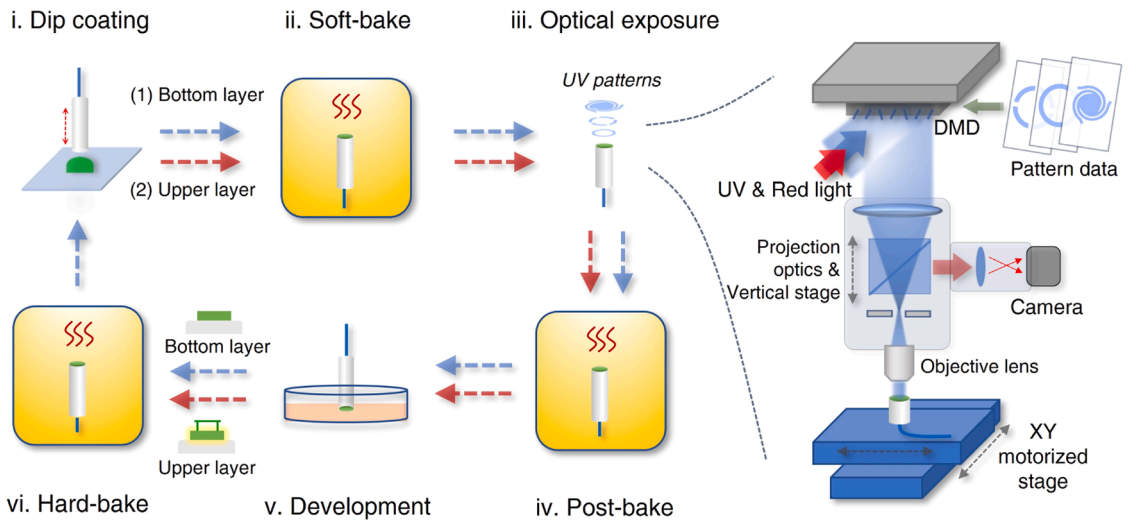

Fig. 2. Flow chart of the optical 3D micro-printing processes for fabricating the optical fiber ferrule-top OMRs. The processes are repeated twice for the fabrication of the bottom and upper layers of the OMRs, respectively. The right part is the schematic of maskless UV exposure system used in optical exposure process.

methyl nonafluorobutyl ether ($C_5H_3F_9O$) to maximally maintain 3D structure [30]. The UV light intensity used in the experiments was about 18.2 mW/mm^2, and the exposure times for the bottom and upper layers were about 150 s and 300 s, respectively.

2.3. Numerical simulation

Mechanical responses of the designed PSS-OMRs were numerically analyzed by using a commercial finite element method (FEM) software, i.e., COMSOL Multiphysics. The Young's modulus and Poisson ratio of SU-8 resin used in simulation are 3.4 GPa and 0.22, respectively [31]. Material intrinsic loss was included as a damping in numerical simulations. Solid mechanics and pressure acoustics analysis were conducted to analyze the induced displacement and eigenfrequencies of the designed PSS-OMRs, respectively.

2.4. Experimental setup for testing the acoustic responses of optical fiber PSS-OMRs

Acoustic responses of the fabricated optical fiber PSS-OMRs were tested in air by using a home-made setup, as shown in Fig. S1. A piezo loudspeaker (Kemo L010) driven by a signal generator was used to generate the excitation acoustic/ultrasonic waves (up to 60 kHz). Although different techniques can be applied to measure the acoustic responses of FP interferometer (FPI) sensors such as spectral demodulation method [32,33], we employed a narrow-linewidth laser based intensity demodulation method for the measurement of high-frequency acoustic responses. The laser's wavelength was tuned to a quadrature point of the PSS-OMR's reflection spectrum. The reflected light was coupled to a photodiode (PD) via a circulator, and the light intensity variation was converted to electric signal and analyzed by a digital oscilloscope. The passband of the PD was set to the range from 1 kHz to 100 kHz. A commercial microphone (B&K 4939) was mounted near the optical fiber PSS-OMR sensor to measure acoustic pressure for calibration. The piezo loudspeaker, the optical fiber PSS-OMR sensor, and the calibration microphone were placed in an acoustic isolation box to suppress the noise influence from external environment.

2.5. Experimental setup for testing optical fiber OMR-PAS gas sensors

The fabricated optical fiber OMR-PAS gas sensor was tested by using a pump-probe experimental setup, as shown in Fig. 3. The pump laser beam was from a 1533-nm distributed feedback (DFB) laser and amplified by an erbium-doped fiber amplifier (EDFA). The probe beam

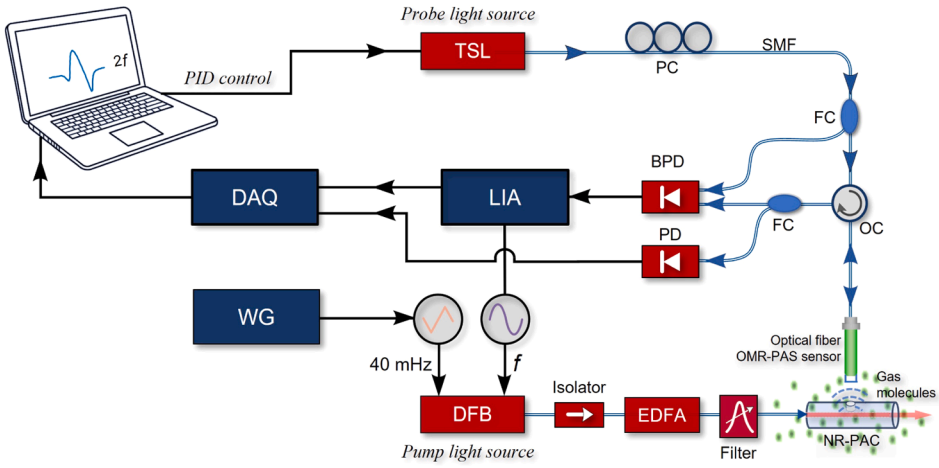

Fig. 3. Schematic diagram of the experimental setup for testing the performances of optical fiber OMR-PAS gas sensors. TSL: tunable semiconductor laser; PC: polarization controller; SMF: single-mode optical fiber; FC: fiber-optic coupler; OC: optical circulator; PD: photodetector; BPD: Balanced photodetector; LIA: lock-in amplifier; DAQ: data acquisition card; WG: waveform generator; DFB: distributed feedback laser; EDFA: erbium-doped fiber amplifier.

was generated by a tunable semiconductor laser (TSL) whose output wavelength can be tuned across the wavelength range from 1500 to 1630 nm. In the experiments, the probe wavelength was adjusted via proportional-integral-derivative (PID) controller to stabilize the interferometer at quadrature. It was slowly scanned across the absorption line $P(13)$ of C_2H_2 gas, and meanwhile was modulated sinusoidally at a higher frequency of $f = \sim 7.35$ kHz to produce acoustic wave. Gas concentration measurement was conducted through a combination of wavelength modulation and second harmonic ($2f$) detection techniques. The PAS signal was demodulated by using a commercial lock-in amplifier (MFLI 500 kHz, Zurich Instruments) with a frequency range of $0 \sim 500$ kHz.

2.6. Preparation of gas samples

Gas mixtures with different concentrations were prepared by mixing calibrated gas samples at ambient temperature and atmospheric pressure with 2 mass flow controllers. For gas concentrations below or equal 103 parts per million (ppm), the gas samples were prepared by mixing the calibrated 103 ppm C_2H_2 with high-purity N_2 in different ratios. For gas concentrations above 103 ppm, the samples were prepared by mixing calibrated 1000 ppm C_2H_2 with high-purity N_2 gas.

3. Results

3.1. Design and simulation results

As shown in Fig. 1**(a)**, the central part of the planar spiral spring is a circular microdisk suspended with three spring arms (i.e., spiral cantilevers). It acts as a partial reflection mirror and forms a micrometre-scale FPI together with the end-face of an input optical fiber, for laser interferometric interrogation of PAS signal. The microdisk is relatively thinner to minimize its additional cavity effect on the reflection spectrum of the FPI. One of the key features of our OMR design is the planar spiral spring. Analogous to the microengineering of supporting microbeams for improving sensitivity and tailoring the resonant frequency in accelerometers [34,35], we use the planar-spiral springs to engineer the vibration resonant modes of the PSS-OMR for resonant PAS gas sensing. It can not only enhance the sensitivity by increasing the effective length of cantilevers but also reduce the size of the entire structure for sensor minimization.

The PAS gas sensor microsystem based on such an optical fiber PSS-OMR is shown in Fig. 1**(b)**. A laser beam whose wavelength matches with a gas absorption line is employed to pump gas samples inside a non-resonant PAC, which can ensure minimal gas consumption and enhance PAS signal. When target gas molecules occur, the absorption of laser beam by target gas will generate a weak acoustic signal whose frequency is determined by the modulation frequency of the pump laser. If the modulation frequency is set to be the resonant frequency of the ferrule-top PSS-OMR, the OMR will be resonantly excited to vibrate at the same frequency. As it acts simultaneously as the reflection mirror of FPI, the PAS signal can then be interferometrically read out by using a probe laser. The miniaturized design of PAS gas sensor can enable the sensor to not only detect gas species in space-constrained environments but also make the microsystem with multiple pump lasers of different wavelengths for simultaneous monitoring of multiple-component gases.

If we model the spring arm as a straightened cantilever, the mechanical response of the PSS-OMR, which is fixed at one end and the other end is constrained and cannot rotate, can be described by using a pseudo-rigid-body model [36]. The spring arm can then be simplified to be a fixed-guided beam and works as a torsional spring. Therefore, under small-deflection assumption, the displacement Δz of the central microdisk, i.e., the change of FP cavity length, of the planar spiral spring with three spring arms for an applied pressure P is

$$\Delta z = \frac{PA \cdot L^3}{6K_\theta EI} \tag{1}$$

where A is the area of the microdisk, L is the length of spring arm, K_θ is the stiffness coefficient, E is the Young's modulus, and I is the area moment of inertia. From the equation, one can see that the pressure sensitivity of the optical fiber PSS-OMR depends on not only the area of micro-disk but also the third power of spring arm length, which reveals the importance of the spiral design on the sensitivity enhancement.

Numerical simulations using COMSOL Multiphysics have been conducted to analyze the mechanical responses of two OMR designs, i.e., PSS-OMR 1 and PSS-OMR 2, with different lengths of spring arms. The outer diameter of the PSS-OMRs is 400 μm, and the diameter of their central parts, i.e., suspended microdisks, is ~200 μm. The width and thickness of the spring arms are set to 25 μm and 10 μm, respectively, which are chosen to compromise with our current optical 3D micro-printing processes. The lengths of the spring arms of PSS-OMR 1 and PSS-OMR 2 are 434 μm and 328 μm, respectively. Numerical simulation results revealed that the displacements of the suspended microdisks of PSS-OMR 1 and PSS-OMR 2 are 17.1 nm and 7.5 nm, respectively, when a static pressure of 1 Pa was applied. As shown in Fig. S2, the displacement of the microdisk, representing the mechanical sensitivity of PSS-OMRs, is linearly proportional to the cube of the length of spring arms, which agrees well with the prediction by Eq. 1. Obviously, the microdisk's displacement also depends on the thickness and width of the spring arms. Figure S3 presents the simulated displacements of microdisks for PSS-OMRs with spring arms of varying widths and thicknesses under a 1-Pa acoustic pressure. The simulated frequency responses of the two PSS-OMRs are given in Figs. 4**(a)** and 4**(d)**, respectively. One can see that the suspended microdisks move vertically by 640 nm and 298 nm, respectively, under the excitation of acoustic pressure of 1 Pa at their resonant frequencies, from which the significance of resonant vibrations on sensitivity enhancement could be clearly seen.

3.2. 3D micro-printed optical fiber ferrule-top PSS-OMRs

The designed PSS-OMRs were directly printed on the end-face of a 1.25 mm-diameter, 10 mm-long fiber-optic ferrule by using our in-house 3D micro-printing technology [29,37,38]. A detailed description of the fabrication processes is provided in **Materials and Methods** part. Figs. 4**(b) and** 4**(e)** show the SEM images of the fabricated optical fiber ferrule-top PSS-OMR 1 and PSS-OMR 2. They contain two layers: the bottom layer is a pedestal to support upper structure and enhance the cavity length of FP interferometer, while the upper layer is the main body of the PSS-OMR. To allow the PSS-OMR to vibrate freely without touching the pedestal, three pillars were introduced to support the spring arms and the microdisk. For the central part of the microdisk, a shallow trail could be observed around circumference, see the inset of Figs. 4**(b) and** 4**(e),** when its thickness is relatively thin. All the fabricated PSS-OMRs have smooth surfaces, and their dimension agrees well with the design. The upper layers of the PSS-OMRs are well aligned with the supporting pedestal and thereby make their reflection microdisks right above the fiber core to form FPI microcavities. These fabrication results demonstrate the high flexibility of 3D micro-printing technology in microengineering the structure of PSS-OMRs at the micrometer scale.

The insets of Figs. 4**(c)** and 4**(f)** show the reflection spectra of the PSS-OMR 1 and PSS-OMR 2, respectively, which are measured by a broadband light source and an optical spectrum analyzer with a resolution of 0.1 nm. The maximum fringe contrasts are ~18 dB and ~14 dB at the spectral measurement spans of PSS-OMR 1 and PSS-OMR 2, respectively. The corresponding fast Fourier transform (FFT) results, also shown in Figs. 4**(c)** and 4**(f)**, indicate that the cavity lengths for both are ~100 μm, which agrees well with the design value.

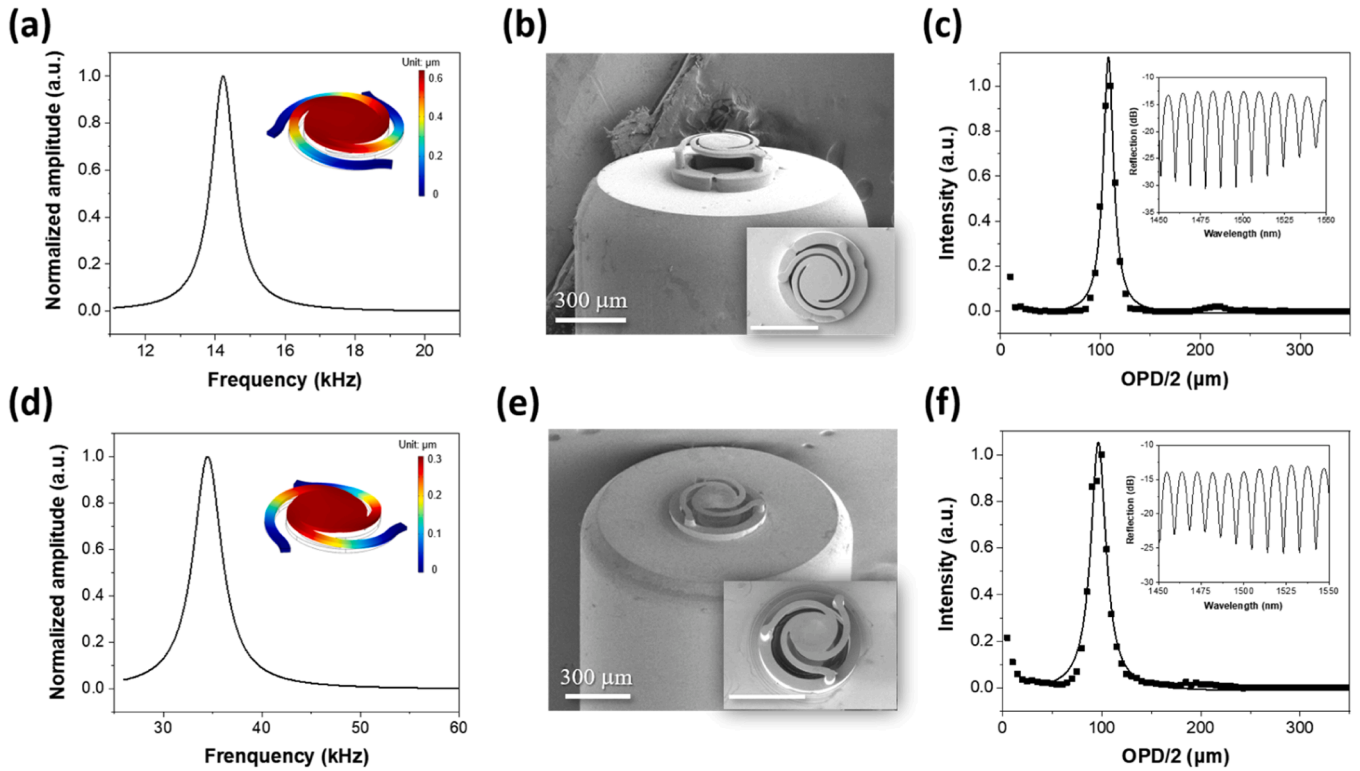

Fig. 4. Simulation and fabrication results of two optical fiber ferrule-top OMRs. (**a**) Simulated frequency response of OMR 1. The inset shows its fundamental vibration mode. (**b**) SEM image of the fabricated OMR 1. (**c**) FFT result of the measured reflection spectrum (given in the inset) of OMR 1. (**d**) Simulated frequency response of OMR 2. The inset shows its fundamental vibration mode. (**e**) SEM image of the fabricated OMR 2. (**f**) FFT result of the measured reflection spectrum (given in the inset) of OMR 2. All scale bars in (B) and (E) have a length of 300 μm.

3.3. Results of the PSS-OMRs' acoustic responses

Fig. 5 shows the measured acoustic responses of the fabricated PSS-OMR 1 and PSS-OMR 2. From the frequency response given in Figs. 5**(a)** and 5**(d)**, one can see that the resonant frequencies of the fundamental vibration mode for PSS-OMR 1 and PSS-OMR 2 are ~14.7 kHz and ~34.5 kHz, respectively. The insets in the two figures show a comparison between numerical and experimental results, whose good consistency indicates the accuracy and reliability of the experiments. According to a Lorentzian fitting, the quality factors (i.e., *Q* factor) of the PSS-OMR 1 and PSS-OMR 2 were determined from experimental data to be ~16.4 and ~10.8, respectively.

Figs. 5**(b)** and 5**(e)** show the measured time-domain outputs of the two optical fiber ferrule-top PSS-OMRs at their resonant frequencies, while the corresponding dependences of the signal amplitudes on the applied acoustic pressure are plotted in Figs. 5**(c)** and 5**(f).** The amplitude of output signals increased with the applied acoustic pressure, showing a linear relationship. The acoustic sensitivity for PSS-OMR 1 is calculated to be ~870 mV/Pa at a resonant frequency of 14.7 kHz. In comparison, the sensitivity measured at a non-resonant frequency of 30 kHz is 8.0 mV/Pa, indicating that micromechanical resonance has led to a ~109-fold amplification in acoustic sensitivity. Figure S4 presents the output signal and the corresponding power spectral density for the PSS-OMR 1 when a sinusoidal acoustic pressure of 0.3 Pa at the resonant frequency of 14.7 kHz is applied. The SNR is ~39.6 dB, from which the estimated noise equivalent acoustic sensitivity is about 147 $\mu Pa/Hz^{1/2}$. For PSS-OMR 2, its sensitivity to applied acoustic pressure was 103.4 mV/Pa at resonant frequency. Compared with its sensitivity at non-resonant frequency, i.e., 3.1 mV/Pa, one can see that the micromechanical vibration resonance has amplified the PSS-OMR's sensitivity by a factor of 33.

3.4. Results of trace-gas detection

The optical fiber PAS gas sensor was fabricated using PSS-OMR 1 and tested using an experimental setup shown in Fig. 3. A non-resonant PAC was used to minimize gas sample consumption and confine the generated acoustic signal. It is a 5-mm long silica glass capillary tube with an inner diameter of ~600 μm, in the middle of which has a femtosecond laser-fabricated hole with a diameter of ~500 μm. The volume of the non-resonant PAC is then calculated to be ~1.4 μL, which is 1 ~ 2 orders of magnitude smaller than that of traditional PACs.

The detection limit of the optical fiber OMR-PAS gas sensor was tested by continuously injecting N_2-balanced 1000-ppm C_2H_2 into the PAC. Fig. 6**(a)** shows the 2*f* (i.e., 14.7 kHz corresponds to resonant frequency of the sensor) lock-in output signals obtained by scanning the pump wavelength across the *P*(13) line of C_2H_2 at different input pump power levels with a lock-in time constant of 200 ms and a filter slope of 18 dB/Oct, corresponding to a detection bandwidth of 0.469 Hz. The corresponding peak-to-peak value of the 2*f* signal (i.e., PAS signal) against the input pump power level is shown in Fig. 6**(b)**. The PAS signal amplitude increases approximately linearly with pump power. The system noise is measured when the pump wavelength is fixed at the *P*(13) line and the sensor is exposed to air. The standard deviation (S.D.) of the noise (1σ noise) with and without pump laser operation is shown in Fig. 6**(c)**. The 1σ noise values are very close, indicating that the noise level changes little with increasing pump power. When the input pump power is 390 mW, the SNR for 1 s lock-in time constant is calculated to be ~4776, whose corresponding noise equivalent concentration (NEC) and noise equivalent absorption (NEA) are 209 ppb C_2H_2 and $\sim 2.2\times10^{-7}$ cm^{-1}, respectively. Lower detection limits can be achieved by delivering higher pump powers to the PAC.

To further assess the minimum NEC of the fabricated optical fiber sensor for C_2H_2 gas detection, we performed an Allan-Werle deviation

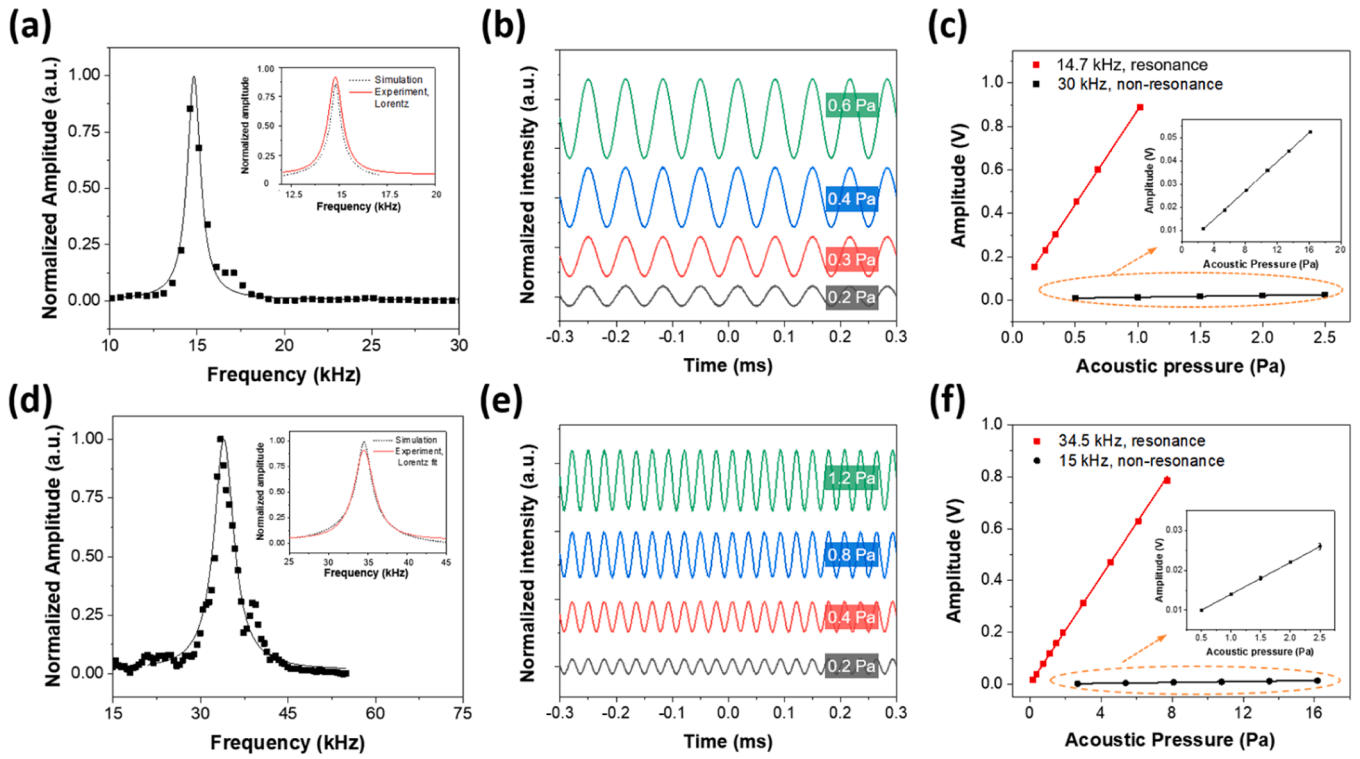

Fig. 5. Measured acoustic responses of the two fabricated optical fiber OMRs. **(a)** The measured frequency response of OMR 1 under 0.2-Pa acoustic excitation. The inset is a comparison between experimental and simulation results. **(b)** The measured waveforms of OMR 1 at resonant frequency under the acoustic pressures of 0.2, 0.3, 0.4, 0.6 Pa, respectively. **(c)** A comparison of the output amplitude of OMR 1 working at resonant and non-resonant frequencies. **(d)** The measured frequency response of OMR 2 under 0.5-Pa acoustic excitation. The inset is a comparison between experimental and simulation results. **(e)** The measured waveforms of OMR 2 at resonant frequency under the acoustic pressures of 0.2, 0.4, 0.8, 1.2 Pa, respectively. **(f)** A comparison of the output amplitude of OMR 2 working at resonant and non-resonant frequencies.

analysis [39–41] based on the noise data over a period of 1 hour. Fig. 6 **(d)** shows the analysis result as a function of the integration time. The NEC decreases with the increase of integration time up to 280 seconds, at which the NEC reaches a minimum of 45 ppb C_2H_2, corresponding to a NEA of 4.7×10^{-8} cm^{-1}. When the integration times are 10 and 100 seconds, the NECs are 206 ppb and 68 ppb C_2H_2, respectively. Notably, all these experiments were conducted at room temperature. For the testing at other temperatures, the effect of temperature variation on PAS signals needs to be reevaluated as both the physical properties of C_2H_2 gas and the thermal characteristics of gas medium are temperature-dependent [42,43]. By comparison, humidity change may have negligible impact, since the relaxation time of C_2H_2 gas sample is not directly affected by H_2O [44].

The dynamic range of the optical fiber OMR-PAS sensor was tested by injecting different concentrations of C_2H_2 into the PAC. Fig. 7**(a)** shows the peak-to-peak value of the 2*f* signal as a function of C_2H_2 concentration when the pump power is 390 mW. From the measured results, the peak-to-peak value and C_2H_2 concentration from 10 to 1000 ppm can be fitted to a linear relationship. The 2*f* signals for 10, 26, 55, 78 ppm C_2H_2 are present as an inset in Fig. 7**(a)**. The response time of the fabricated sensor was tested by rapidly switching off and on 1000-ppm C_2H_2 gas at a flow rate of 265 standard cm^3/min. Fig. 7**(b)** shows the testing result in which the signal has been normalized by removing the baseline and scaling them against the maximum value. The jump in 2*f* signal is due to the change in the working point of the interferometer caused by the gas flow. The measured response times, specifically the times required for reaching 90 % (i.e., rise time) and descending to 10 % (i.e., fall time) of the maximum 2*f* signal, are about 0.20 ~ 0.26 seconds.

4. Discussion and conclusion

It is known that a miniaturized non-resonant PAC can enhance PAS signal by reducing the consumption of sample gas and directional emission of acoustic waves [28]. To reveal its function in our experimental results, we have experimentally evaluated the effect of different kinds of non-resonant PACs including copper and silica glass micro-tubes, as shown in Fig. S5, on PAS signals. The detailed geometric parameters of different PACs are provided in Table S1. In the experiments, 1000-ppm C_2H_2 gas was continuously injected into the PACs, and the PAS signals are generated at a pump modulation frequency of ~7.35 kHz.

As shown in Fig. S6**(a)**, compared to direct detection without PAC, both 5-mm-long copper and glass PACs can enhance the PAS signal by ~5 times. Slight differences in PAS signals for the two same-volume PACs may result from manufacturing non-uniformities of their inner walls. However, a background noise floor was observed when the sensor was tested together with the copper PAC, as shown in Fig. S6**(b)**. This noise is likely due to light absorption by the cell walls. Since silica glass is transparent in the near-infrared range, the background noise is much smaller.

Notably, although the fabricated optical fiber OMR-PAS sensor was demonstrated to detect C_2H_2 gas sensor, the key part of the sensor, i.e., optical fiber ferrule-top PSS-OMRs, is generally a high-sensitivity opto-mechanical acoustic sensor that can be readily adapted for detection of other gases by integrating it with a pump laser operating at a different wavelength. Moreover, it can be conveniently extended to make a compact optical OMR-PAS gas detection microsystem to detect multiple gas species in case that a wavelength-tunable pump laser or multiple pump lasers are utilized to work with the optical fiber ferrule-top PSS-OMR for PAS gas sensing. A comparison of our sensor with recently

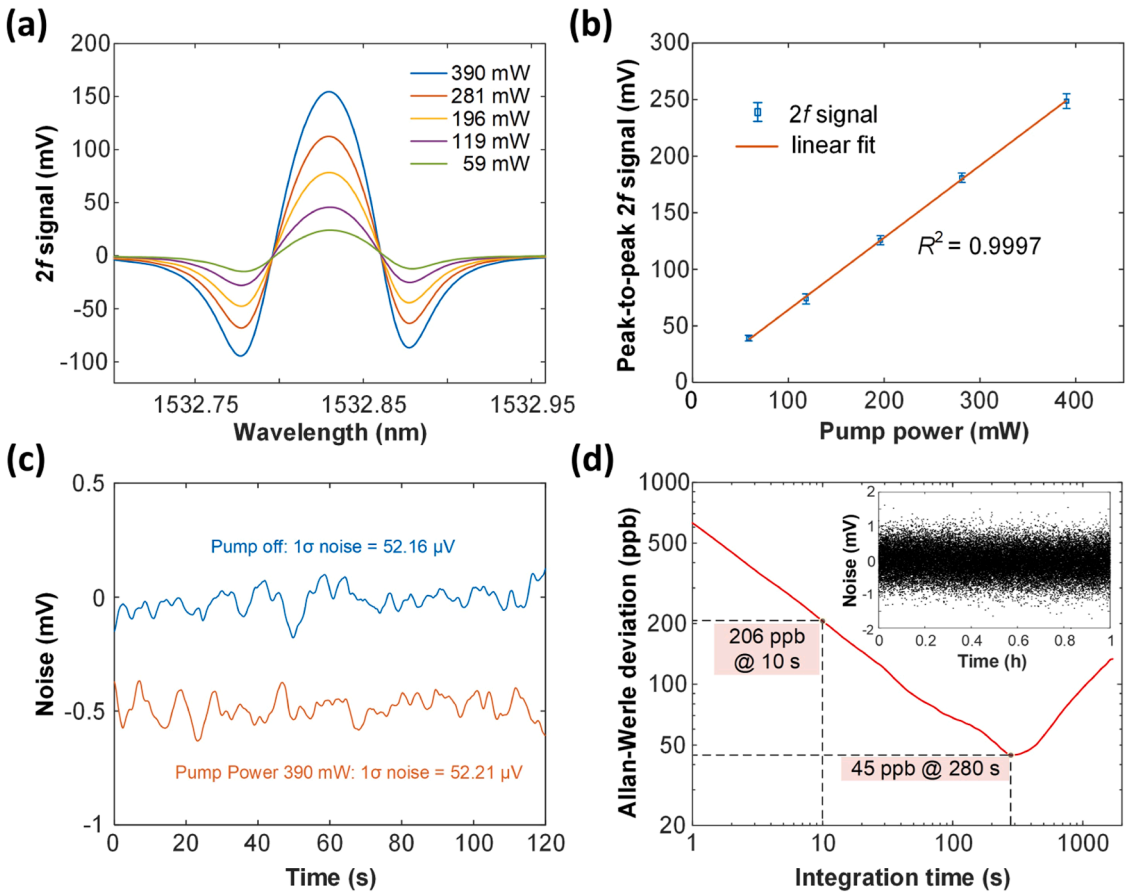

Fig. 6. Results of detection limit tests. **(a)** Measured 2 *f* signals for 1000-ppm C_2H_2 at different input pump power levels with a detection bandwidth of 0.469 Hz. **(b)** Peak-to-peak value of the 2 *f* signals as a function of input pump power levels. Error bars for 2 *f* signal show the S.D. of 5 measurements, and the magnitudes of the error bars are scaled up by 15-fold for clarity reason. **(c)** The 1σ noise for different pump powers when the pump wavelength is fixed at the *P*(13) line and the detection bandwidth is 0.094 Hz. Blue line is the result when pump power is zero (off). Orange line: pump power is ~390 mW (on), and the 1σ noise was shifted down by 0.5 mV for easy comparison. **(d)** Allan-Werle deviation plot based on the noise data (detection bandwidth of 3.125 Hz) over a period of 1 h.

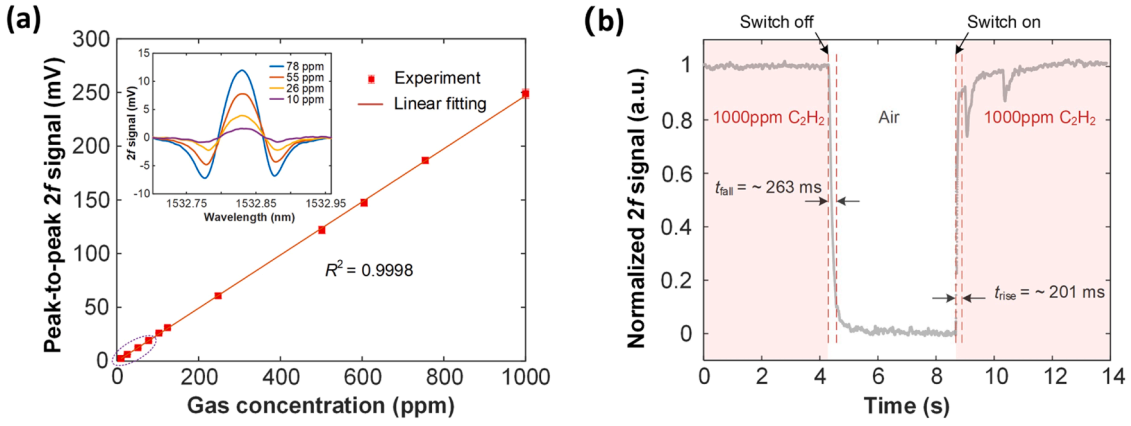

Fig. 7. Results of dynamic range and response time tests. **(a)** Peak-to-peak value of the 2 *f* signal as a function of gas concentration. Error bars show the S.D. from 5 measurements and their magnitudes are scaled up 10 times for better clarity. Inset: 2 *f* signals when pump wavelength is tuned across the *P*(13) line for 10, 26, 55, 78 ppm C_2H_2 at room temperature and atmospheric pressure and detection bandwidth is 0.094 Hz. **(b)** Response time testing result. 1000-ppm C_2H_2 gas was unloaded at ~ 4.3 s and loaded at ~8.7 s under the flow rate of 265 standard cm^3/min. Data in (b) was measured with a detection bandwidth of 9.4 Hz.

reported PAS sensors is given in Table 1, showing that our PSS-OMR gas sensor has not only the advantage of small size but also comparable or better performances in terms of gas consumption, detection limit and response time.

In conclusion, we have demonstrated an ultracompact optical fiber optomechanical resonant PAS gas sensor based on a micrometer-scale PSS-OMR that is *in situ* 3D micro-printed on the end face of a fiber-optic ferrule. As it is an inherently light-coupled microscopic platform, the proposed sensor design can efficiently overcome the tradeoff between small size and high sensitivity to develop ultrasensitive miniaturized optical fiber PAS gas sensors. In the experiments, an optical fiber OMR-PAS gas sensor whose sensor head is as small as 400 μm in

Table 1
Performance comparison between our optical fiber OMR-PAS gas sensor and recently reported PAS sensors.

Ref.	Acoustic Sensing Element	PAC	Integration Time (s)	Detection Limit	Response Time (s)
[45]	Capacitive microphone	7.9 mL[#] Resonant PA tube	3	8.7 ppm (H_2O)	> 20[#]
[46]	Quartz tuning fork	272 mL Multi-pass cell	140	1.29 ppb (C_2H_2)	N.A.
[47]	Cantilever	0.35 mL Helmholtz resonator	100	15 ppb (C_2H_2)	140
[48]	Cantilever	32 μL[#] Non-resonant PA tube	60	0.32 ppm (CH_4)	N.A.
[23]	Diaphragm	Free space	32	119.8 ppb (C_2H_2)	N.A.
[24]	Diaphragm	6.0 mL[#] Resonant PA tube	81	4.87 ppb (CH_4)	N.A.
[25]	Diaphragm	Compact multi-pass cell	100	50 ppb (C_2H_2)	N.A.
[28]	Cantilever	0.56 mL Non-resonant PA tube	60	199.8 ppt (C_2H_2)	N.A.
This work	PSS-OMR	1.4 μL Non-resonant PA tube	280	45 ppb (C_2H_2)	< 0.3

[#] Data were calculated based on the related cited work.

diameter has been fabricated to detect the concentration of C_2H_2 gas at the 45-ppb level. It holds the promise of monitoring fast-varying trace gases as its response time is as short as 0.2 second. Such a small-size high-sensitivity optical fiber gas sensor provides a new trace-gas detection technology for various applications such as environmental monitoring and industrial process controls.

Funding

The work was fully supported by a grant from the Research Grants Council of the Hong Kong SAR, China (Grant No.: 15221119) and the Local Innovative and Research Teams Project of Guangdong Pearl River Talents Program (Grant No.: 2019BT02X105).

CRediT authorship contribution statement

Taige Li: Writing – original draft, Validation, Investigation. **Pengcheng Zhao:** Writing – original draft, Validation, Investigation. **Peng Wang:** Writing – review & editing, Validation, Investigation. **Kummara Venkata Krishnaiah:** Writing – review & editing, Investigation. **Wei Jin:** Writing – review & editing, Validation, Supervision, Data curation. **A. Ping Zhang:** Writing – original draft, Supervision, Methodology, Investigation, Funding acquisition, Conceptualization.

Declaration of Competing Interest

The authors declare that they have no known competing financial interests or personal relationships that could have appeared to influence the work reported in this paper.

Appendix A. Supporting information

Supplementary data associated with this article can be found in the online version at doi:10.1016/j.pacs.2024.100657.

Data Availability

No data was used for the research described in the article.

References

[1] C. Hagleitner, A. Hierlemann, D. Lange, A. Kummer, N. Kerness, O. Brand, H. Baltes, Smart single-chip gas sensor microsystem, Nature 414 (2001) 293–296, https://doi.org/10.1038/35104535.
[2] D.I. Herman, C. Weerasekara, L.C. Hutcherson, F.R. Giorgetta, K.C. Cossel, E. M. Waxman, G.M. Colacion, N.R. Newbury, S.M. Welch, B.D. DePaola, I. Coddington, E.A. Santos, B.R. Washburn, Precise multispecies agricultural gas flux determined using broadband open-path dual-comb spectroscopy, Sci. Adv. 7 (2021) eabe9765, https://doi.org/10.1126/sciadv.abe9765.
[3] L.Y. Stein, M.E. Lidstrom, Greenhouse gas mitigation requires caution, Science 384 (2024) 1068–1069, https://doi.org/10.1126/science.adi0503.
[4] J. Hodgkinson, R.P. Tatam, Optical gas sensing: a review, Meas. Sci. Technol. 24 (2013) 012004, https://doi.org/10.1088/0957-0233/24/1/012004.
[5] W. Jin, Y. Cao, F. Yang, H.L. Ho, Ultra-sensitive all-fibre photothermal spectroscopy with large dynamic range, Nat. Commun. 6 (2015) 6767, https://doi.org/10.1038/ncomms7767.
[6] D.A. Long, M.J. Cich, C. Mathurin, A.T. Heiniger, G.C. Mathews, A. Frymire, G. B. Rieker, Nanosecond time-resolved dual-comb absorption spectroscopy, Nat. Photon. 18 (2024) 127–131, https://doi.org/10.1038/s41566-023-01316-8.
[7] T. Yang, W. Chen, P. Wang, A review of all-optical photoacoustic spectroscopy as a gas sensing method, Appl. Spectrosc. Rev.. 56 (2020) 143–170, https://doi.org/10.1080/05704928.2020.1760875.
[8] J. Karhu, T. Hieta, F. Manoocheri, M. Vainio, E. Ikonen, LED-Based Photoacoustic NO_2 Sensor with a Sub-ppb Detection Limit, ACS Sens 6 (2021) 3303–3307, https://doi.org/10.1021/acssensors.1c01073.
[9] Y. Yin, D. Ren, C. Li, R. Chen, J. Shi, Cantilever-enhanced photoacoustic spectroscopy for gas sensing: A comparison of different displacement detection methods, Photoacoustics 28 (2022) 100423, https://doi.org/10.1016/j.pacs.2022.100423.
[10] A. Fathy, Y.M. Sabry, I.W. Hunter, D. Khalil, T. Bourouina, Direct Absorption and Photoacoustic Spectroscopy for Gas Sensing and Analysis: A Critical Review, Laser Photonics Rev. 16 (2022) 2100556, https://doi.org/10.1002/lpor.202100556.
[11] A. Lay-Ekuakille, G. Vendramin, A. Trotta, LED-based sensing system for biomedical gas monitoring: Design and experimentation of a photoacoustic chamber, Sens. Actuators B Chem. 135 (2009) 411–419, https://doi.org/10.1016/j.snb.2008.09.041.
[12] D. Mitrayana, D.K. Apriyanto, M. Satriawan, CO_2 Laser Photoacoustic Spectrometer for Measuring Acetone in the Breath of Lung Cancer Patients, Biosensors 10 (2020) 55, https://doi.org/10.3390/bios10060055.
[13] X. Yin, L. Dong, H. Wu, L. Zhang, W. Ma, W. Yin, L. Xiao, S. Jia, F.K. Tittel, Highly sensitive photoacoustic multicomponent gas sensor for SF_6 decomposition online monitoring, Opt. Express 27 (2019) A224–A234, https://doi.org/10.1364/OE.27.00A224.
[14] A. Szabó, Á. Mohácsi, G. Gulyás, Z. Bozóki, G. Szabó, In situ and wide range quantification of hydrogen sulfide in industrial gases by means of photoacoustic spectroscopy, Meas. Sci. Technol.. 24 (2013) 065501, https://doi.org/10.1088/0957-0233/24/6/065501.
[15] H. Huszár, A. Pogány, Z. Bozóki, Á. Mohácsi, L. Horváth, G. Szabó, Ammonia monitoring at ppb level using photoacoustic spectroscopy for environmental application, Sens. Actuators B Chem. 134 (2008) 1027–1033, https://doi.org/10.1016/j.snb.2008.05.013.
[16] A. Zifarelli, R. De Palo, P. Patimisco, M. Giglio, A. Sampaolo, S. Blaser, J. Butet, O. Landry, A. Müller, V. Spagnolo, Multi-gas quartz-enhanced photoacoustic sensor for environmental monitoring exploiting a Vernier effect-based quantum cascade laser, Photoacoustics 28 (2022) 100401, https://doi.org/10.1016/j.pacs.2022.100401.
[17] Y. Ma, S. Qiao, P. Patimisco, A. Sampaolo, Y. Wang, F.K. Tittel, V. Spagnolo, In-plane quartz-enhanced photoacoustic spectroscopy, Appl. Phys. Lett. 116 (2020) 061101, https://doi.org/10.1063/1.5142330.
[18] J. Wang, H. Wu, A. Sampaolo, P. Patimisco, V. Spagnolo, S. Jia, L. Dong, Quartz-enhanced multiheterodyne resonant photoacoustic spectroscopy, Light Sci. Appl. 13 (2024) 77, https://doi.org/10.1038/s41377-024-01425-1.
[19] A. Sampaolo, P. Patimisco, M. Giglio, A. Zifarelli, H. Wu, L. Dong, V. Spagnolo, Quartz-enhanced photoacoustic spectroscopy for multi-gas detection: A review, Anal. Chim. Acta 1202 (2022) 338894, https://doi.org/10.1016/j.aca.2021.338894.
[20] H. Wu, L. Dong, H. Zheng, Y. Yu, W. Ma, L. Zhang, W. Yin, L. Xiao, S. Jia, F. Tittel, Beat frequency quartz-enhanced photoacoustic spectroscopy for fast and calibration-free continuous trace-gas monitoring, Nat. Commun. 8 (2017) 15331, https://doi.org/10.1038/ncomms15331.
[21] S. Qiao, A. Sampaolo, P. Patimisco, V. Spagnolo, Y. Ma, Ultra-highly sensitive HCl-LITES sensor based on a low-frequency quartz tuning fork and a fiber-coupled multi-pass cell, Photoacoustics 27 (2022) 100381, https://doi.org/10.1016/j.pacs.2022.100381.
[22] J. Zhao, Y. Pan, P. Lu, X. Zhang, T. Li, J. Zhang, C. Sima, D. Liu, Ppb-level all-optical off-axis QEPAS gas sensor based on dual-wavelength demodulation of out-

of-plane vibration mode, Sens. Actuators B Chem. 385 (2023) 133689, https://doi.org/10.1016/j.snb.2023.133689.
[23] Y. Tan, C. Zhang, W. Jin, F. Yang, H.L. Ho, J. Ma, Optical Fiber Photoacoustic Gas Sensor With Graphene Nano-Mechanical Resonator as the Acoustic Detector, IEEE J. Sel. Top. Quantum Electron. 23 (2017) 199–209, https://doi.org/10.1109/JSTQE.2016.2606339.
[24] H. Xiao, J. Zhao, C. Sima, P. Lu, Y. Long, Y. Ai, W. Zhang, Y. Pan, J. Zhang, D. Liu, Ultra-sensitive ppb-level methane detection based on NIR all-optical photoacoustic spectroscopy by using differential fiber-optic microphones with gold-chromium composite nanomembrane, Photoacoustics 26 (2022) 100353, https://doi.org/10.1016/j.pacs.2022.100353.
[25] E. Fan, H. Liu, C. Wang, J. Ma, B.O. Guan, Compact optical fiber photoacoustic gas sensor with integrated multi-pass cell, Photoacoustics 32 (2023) 100524, https://doi.org/10.1016/j.pacs.2023.100524.
[26] S. Zhou, M. Slaman, D. Iannuzzi, Demonstration of a highly sensitive photoacoustic spectrometer based on a miniaturized all-optical detecting sensor, Opt. Express 25 (2017) 17541–17548, https://doi.org/10.1364/OE.25.017541.
[27] C. Li, M. Guo, B. Zhang, C. Li, B. Yang, K. Chen, Miniature single-fiber photoacoustic sensor for methane gas leakage detection, Opt. Laser Eng. 149 (2022) 106792, https://doi.org/10.1016/j.optlaseng.2021.106792.
[28] M. Guo, K. Chen, C. Li, L. Xu, G. Zhang, N. Wang, C. Li, F. Ma, Z. Gong, Q. Yu, High-Sensitivity Silicon Cantilever-Enhanced Photoacoustic Spectroscopy Analyzer with Low Gas Consumption, Anal. Chem. 94 (2022) 1151–1157, https://doi.org/10.1021/acs.analchem.1c04309.
[29] M. Yao, Y. Zhang, X. Ouyang, A.P. Zhang, H.Y. Tam, P.K.A. Wai, Ultracompact optical fiber acoustic sensors based on a fiber-top spirally-suspended optomechanical microresonator, Opt. Lett. 45 (2020) 3516–3519, https://doi.org/10.1364/OL.393900.
[30] X. Shang, N. Wang, S. Cao, H. Chen, D. Fan, N. Zhou, M. Qiu, Fiber-Integrated Force Sensor using 3D Printed Spring-Composed Fabry-Perot Cavities with a High Precision Down to Tens of Piconewton, Adv. Mater. 36 (2024) e2305121, https://doi.org/10.1002/adma.202305121.
[31] H. Lorenz, M. Despont, N. Fahrni, N. LaBianca, P. Renaud, P. Vettiger, SU-8: a low-cost negative resist for MEMS, J. Micromech. Microeng. 7 (1997) 121–124, https://doi.org/10.1088/0960-1317/7/3/010.
[32] K. Chen, Z. Yu, Q. Yu, M. Guo, Z. Zhao, C. Qu, Z. Gong, Y. Yang, Fast demodulated white-light interferometry-based fiber-optic Fabry–Perot cantilever microphone, Opt. Lett. 43 (2018) 3417–3420, https://doi.org/10.1364/OL.43.003417.
[33] X. Zhao, H. Qi, Y. Xu, C. Li, M. Guo, K. Chen, Fiber-optic photoacoustic gas sensing: a review, Appl. Spectrosc. Rev. (2024) 1–29, https://doi.org/10.1080/05704928.2024.2359933.
[34] S. Shi, W. Geng, K. Bi, Y. Shi, F. Li, J. He, X. Chou, High Sensitivity MEMS Accelerometer Using PZT-Based Four L-Shaped Beam Structure, IEEE Sens. J. 22 (2022) 7627–7636, https://doi.org/10.1109/JSEN.2022.3155407.
[35] F.A. Bruno, M. Pisco, G. Gruca, N. Rijnveld, A. Cusano, Opto-mechanical lab-on-fiber accelerometers, J. Light. Tech. 38 (2020) 1998–2009, https://doi.org/10.1109/JLT.2019.2961766.
[36] J.J. Parise, L.L. Howell, S.P. Magleby, Ortho-planar linear-motion springs, Mech. Mach. Theory 36 (2001) 1281–1299, https://doi.org/10.1016/S0094-114X(01)00051-9.
[37] P. Zhao, K.V. Krishnaiah, L. Guo, T. Li, H.L. Ho, A.P. Zhang, W. Jin, Ultraminiature Optical Fiber-Tip 3D-Microprinted Photothermal Interferometric Gas Sensors, Laser Photonics Rev. 18 (2024) 2301285, https://doi.org/10.1002/lpor.202301285.
[38] J. Wu, M. Yao, F. Xiong, A.P. Zhang, H.-Y. Tam, P.K.A. Wai, Optical Fiber-Tip Fabry–Pérot Interferometric Pressure Sensor Based on an In Situ μ-Printed Air Cavity, J. Light. Technol. 36 (2018) 3618–3623, https://doi.org/10.1109/JLT.2018.2843885.
[39] W. Allan, Statistics of atomic frequency standards, Proc. IEEE 54 (1966) 221–230, https://doi.org/10.1109/PROC.1966.4634.
[40] P. Werle, R. Mücke, F. Slemr, The limits of signal averaging in atmospheric trace-gas monitoring by tunable diode-laser absorption spectroscopy (TDLAS), Appl. Phys. B 57 (1993) 131–139, https://doi.org/10.1007/BF00425997.
[41] P. Zhao, Y. Zhao, H. Bao, H.L. Ho, W. Jin, S. Fan, S. Gao, Y. Wang, P. Wang, Mode-phase-difference photothermal spectroscopy for gas detection with an anti-resonant hollow-core optical fiber, Nat. Commun. 11 (2020) 847, https://doi.org/10.1038/s41467-020-14707-0.
[42] K. Chen, B. Yang, M. Guo, H. Deng, B. Zhang, S. Liu, C. Li, R. An, W. Peng, Q. Yu, Fiber-optic photoacoustic gas sensor with temperature self-compensation, Opt. Lett. 45 (2020) 2458–2461, https://doi.org/10.1364/OL.390898.
[43] T. Kuusela, J. Kauppinen, Photoacoustic gas analysis using interferometric cantilever microphone, Appl. Spectrosc. Rev. 42 (2007) 443–474, https://doi.org/10.1080/00102200701421755.
[44] J. Pangerl, M. Müller, T. Rück, S. Weigl, R. Bierl, Characterizing a sensitive compact mid-infrared photoacoustic sensor for methane, ethane and acetylene detection considering changing ambient parameters and bulk composition (N_2, O_2 and H_2O), S, Sens. Actuators B Chem. 352 (2022) 130962, https://doi.org/10.1016/j.snb.2021.130962.
[45] S. Qiao, Y. He, H. Sun, P. Patimisco, A. Sampaolo, Vo Spagnolo, Y. Ma, Ultra-highly sensitive dual gases detection based on photoacoustic spectroscopy by exploiting a long-wave, high-power, wide-tunable, single-longitudinal-mode solid-state laser, Light Sci. Appl. 13 (2024) 100, https://doi.org/10.1038/s41377-024-01459-5.
[46] Y. Liu, S. Qiao, C. Fang, Y. He, H. Sun, J. Liu, Y. Ma, A highly sensitive LITES sensor based on a multi-pass cell with dense spot pattern and a novel quartz tuning fork with low frequency, Opto-Electron. Adv. 7 (2024) 230230, https://doi.org/10.29026/oea.2024.230230.
[47] C. Li, X. Han, M. Guo, H. Qi, H. Wang, X. Zhao, K. Chen, Fiber-Optic Photoacoustic Gas Microsensor Dual Enhanced by Helmholtz Resonator and Interferometric Cantilever, Anal. Chem. 96 (2024) 9438–9446, https://doi.org/10.1021/acs.analchem.4c00532.
[48] M. Guo, K. Chen, B. Yang, G. Zhang, X. Zhao, C. Li, Miniaturized anti-interference cantilever-enhanced fiber-optic photoacoustic methane sensor, Sens. Actuators B Chem. 370 (2022) 132446, https://doi.org/10.1016/j.snb.2022.132446.

Taige Li received the B.Eng. degree in electronic engineering from the City University of Hong Kong, Hong Kong, China, in 2020. Currently he is a Ph.D. student at The Hong Kong Polytechnic University (PolyU), Hong Kong, China. His research interests mainly include optomechanical micro-resonators, optical fiber sensors, and optical waveguide sensors.

Pengcheng Zhao is currently a Postdoctoral Fellow at PolyU. He received his Ph.D. from Beihang University in 2022 and B.S. from Jilin University in 2015. He was the recipient of numerous national scholarships and awards, such as Humboldt Research Fellowship for Postdocs and the Best Oral Presentation Awards of OFS-China 2024. His research interests mainly focus on laser spectroscopy, fiber-optic sensors and devices.

Peng Wang received the B.Eng. and M.Eng. degree from the China University of Geosciences, Wuhan, China, and Southeast University, Nanjing, China, in 2020 and 2023, respectively. Currently he is a Ph.D. student at PolyU. His research interests mainly include optical fiber optomechanical sensors, optical fiber accelerometers and MEMS sensors.

Kummara Venkata Krishnaiah received his master's and PhD degrees in physics from the Department of Physics at Sri Venkateswara University, Tirupati, India, in 2008 and 2013, respectively. Currently he is a Research Associate in the Department of Electrical and Electronics Engineering at PolyU. His research interests include optical fiber gas sensors, WGM microlaser biosensors, optical waveguide devices, photodetectors, and optoelectronic devices.

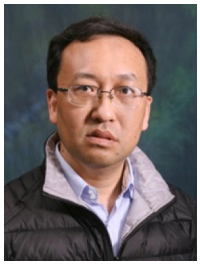

Wei Jin obtained his B.Eng. and M.Sc. degrees from Beijing University of Aeronautics and Astronautics in 1984 and 1987, respectively, and the Ph.D. degree in Optoelectronics from University of Strathclyde, Scotland, UK, in 1991. He currently is the Chair Professor of Photonic Instrumentation at the Department of Electrical and Electronic Engineering of PolyU. He is a Fellow of OPTICA, a Senior Member of IEEE and a director of Chinese Optical Society. His research interests include photonic crystal fiber devices, optical fiber sensors, and optical trace-gas sensor systems.

A. Ping Zhang received the B.Sc. and M.Sc. degrees from Zhejiang University (ZJU), Hangzhou, China, in 1997 and 2000, respectively, and the Ph.D. degree from PolyU, Hong Kong, China, in 2003. He worked as a Research Scholar at State University of New-York at Buffalo (UB) in 2006–2008 and University of California, San Diego (UCSD) in 2011, respectively. Currently he is the Professor at the Department of Electrical and Electronic Engineering of PolyU. He is a Senior Member of IEEE and OPTICA. His research interests include optical micro/nano-fabrication technologies, photonic devices, sensors, and microsystem.